International Journal of Hydrogen Energy 120 (2025) 201–212

Contents lists available at ScienceDirect

International Journal of Hydrogen Energy

journal homepage: www.elsevier.com/locate/he

Study on Ni-ceramic cathode degradation in H_2O electrolysis using a two-dimensional patterned cell

Xiaolin Shao [a,*], Riyan Achmad Budiman [a,b], Takashi Sato [a], Mina Yamaguchi [a], Keiji Yashiro [a,c], Tatsuya Kawada [a]

[a] Graduate School Environmental Studies, Tohoku University, 6-6-01 Aramaki-Aoba, Aoba-ku, Sendai, 980-8579, Japan
[b] Research Center for Advanced Material, National Research and Innovation Agency (BRIN), South Tangerang, Banten, 15314, Indonesia
[c] Faculty of Materials for Energy, Shimane University, 1060 Nishikawatsu, Matsue, Shimane, 690-8504, Japan

ARTICLE INFO

Handling Editor: Fanglin F. Chen

Keywords:
SOEC
Durability test
Cathode degradation
Ni migration

ABSTRACT

The degradation of fuel electrodes in solid oxide electrolysis cells (SOECs) remains a major barrier to their commercialization. The complex electrode structures of conventional cells complicate the study of degradation mechanisms. To address this challenge, this study employed a simplified electrode structure by designing and fabricating a comb shaped patterned cell to examine cathode degradation in SOECs. Yttria-stabilized zirconia (YSZ) and $Ce_{0.9}Gd_{0.1}O_{1.95}$ (GDC) were used as ceramic materials, with varying pattern sizes designed to investigate their reaction characteristics. Electrochemical analysis combined with microstructural characterization revealed that Ni detachment occurred exclusively on the GDC film, contributing to increased ohmic resistance. By contrast, no significant microstructural changes were observed in Ni-YSZ systems. These differences were likely attributed to the higher oxygen vacancy concentration at the GDC interface, resulting from the oxygen nonstoichiometry of the material. Additionally, while ohmic resistance increased, polarization resistance showed comparatively minor changes, suggesting that the reaction degradation was less severe. Further analysis of the pattern size revealed that reactions in the Ni-GDC system were not restricted to the three-phase boundary but extended to the double-phase boundary, highlighting the broader reaction region in these systems.

1. Introduction

Recently, to address environmental concerns, numerous studies have focused on developing cleaner and more efficient energy conversion systems [1–3]. Among these, solid oxide electrolysis cells (SOECs) have gained considerable attention for their ability to convert electricity into chemical energy with high efficiency and selectivity [4,5]. Despite their potential, the critical issue of stability remains a significant hurdle to SOEC commercialization. Long-term SOEC operation is affected by various degradation factors, with cathode degradation being the most extensively studied [6]. SOECs, which operate via the reverse reaction of solid oxide fuel cells (SOFCs), commonly use Ni-yttria-stabilized zirconia (Ni-YSZ) as the fuel electrode material. However, elevated temperatures and high water vapor concentrations can lead to Ni coarsening, which reduces the three-phase boundary (TPB) and increases electrode polarization resistance [7]. Additionally, Ni migration near the electrolyte causes depletion in this region, which not only thickens the electrolyte—thereby increasing ohmic resistance—but also reduces the porosity of the ceramic framework, hindering the diffusion of gas reactants [8]. While various hypotheses have been proposed to explain these degradation phenomena, the precise mechanism driving Ni migration remains elusive. Further investigation into the degradation mechanisms is essential to enhance understanding and facilitate the development of more stable and commercially viable SOEC systems.

In addition to Ni-YSZ, Ni-GDC (Gadolinia-doped Ceria, $Ce_{0.9}Gd_{0.1}O_{1.95}$) has emerged as a promising cermet cathode material for SOEC [9,10]. Compared with YSZ, GDC offers superior ionic conductivity at relatively low temperatures [11,12]. Moreover, under reducing conditions, GDC functions as a mixed ionic and electronic conductor (MIEC). This unique property expands the reaction region from the three-phase boundary (Ni-ceramic-reactant) in Ni-YSZ cathodes to the double-phase boundary (DPB) (ceramic-reactant) in Ni-GDC cathodes, significantly enhancing cathode performance [13,14]. Additionally, studies highlight the importance of surface characteristics, such as oxygen vacancies, in determining cathode performance in SOECs [10,15]. Under reducing conditions, GDC exhibits an increase in surface Ce^{3+}

* Corresponding author.
E-mail address: shao.xiaolin.t8@dc.tohoku.ac.jp (X. Shao).

https://doi.org/10.1016/j.ijhydene.2025.03.236
Received 23 December 2024; Received in revised form 3 March 2025; Accepted 15 March 2025
Available online 26 March 2025

ions, which facilitates the reaction process [15]. Although the exact mechanism remains unclear, it is hypothesized that this behavior is associated with an increase in oxygen vacancies and polarons [15]. The distinct material properties of GDC and YSZ result in varied cell performances and degradation phenomena [14]. For instance, Sciazko et al. reported that both Ni-GDC and Ni-YSZ exhibit common degradation features such as Ni coarsening and migration after prolonged operation. However, Ni-GDC systems uniquely exhibit GDC diffusion, forming a thin layer on the Ni particles [14]. This phenomenon, though not fully understood, is believed to contribute to performance degradation. To address these challenges, this study utilized YSZ and GDC as cathode materials to investigate the influence of their material properties on the degradation phenomenon and explore the possible mechanisms underlying these behaviors.

Although extensive studies have been conducted to elucidate the mechanisms of cathode degradation, progress has reached a bottleneck. The intricate three-dimensional structure of porous materials in conventional or commercial-type cells complicates the distinction of individual factors affecting microstructural evolution. To address this, researchers have turned to novel investigative approaches, such as patterned cells. Unlike conventional cells, patterned cells offer simpler structures [16,17] and enhanced flexibility [18] owing to their highly customizable designs. Shikazono et al. investigated Ni morphology changes under SOFC and SOEC modes using square-patterned cells [19–25]. Their findings indicated that in SOFC mode, increased Ni wettability and coarsening promote Ni diffusion, while in SOEC mode, reduced wettability leads to delamination between Ni and YSZ [21]. Building on these insights, our group recently introduced a two-dimensional comb-shaped patterned cell to study the effects across the electrode thickness [26]. This design enabled the observation of distinct Ni behaviors in fuel cell (FC) and electrolysis cell (EC) modes. In the FC mode, increased oxygen potential in the TPB region and enhanced Ni wettability drove Ni diffusion toward the electrolyte. Conversely, in EC mode, decreased wettability caused Ni to migrate in the opposite direction. The driving force behind these microstructural changes is hypothesized to be adsorbed water vapor, which affects the local oxygen potential [26,27].

This study employed a patterned cell similar to that used in a previous study [26]. Different ceramic cathode materials were utilized to investigate the effect of material properties on morphology changes in the cathode during durability test. Electrochemical performance analysis combined with Ni microstructural characterization was conducted to quantify the effects of these observed changes.

2. Experiment

2.1. Sample preparation

The patterned cell fabrication largely followed the procedure outlined in a previous study [26], as illustrated in Fig. 1(a). The primary difference was the use of a 150 μm YSZ substrate and the application of pulsed laser deposition to coat YSZ and GDC thin films onto the mirror-polished surface. The YSZ pellet was then directly employed for photolithography and patterned electrode fabrication. To minimize the impact of electronic conductivity of GDC under high temperatures [28] and reducing atmospheres on cell performance, the middle section of the GDC between the electrodes was removed using ion beam milling (Hakuto IBE-KDC75) before electrode fabrication (Fig. S(1)). A negative photoresist was then applied to form the Pt anodes (Fig. 1(b)). The photoresist was coated onto the substrate using a spin coater (Mikasa 1H-DXII and Actes ASC-4000), followed by exposure and development to achieve the desired pattern (Maskless Aligner, Heidelberg Instruments MLA150). A 1000 nm Pt film was subsequently deposited via metal sputtering (Shibaura sputtering system, Shibaura Mechatronics CFS-4ESII). Excess Pt was removed using a lift-off process in an N-methylpyrrolidone (NMP) solution at 363–373 K. Ni electrodes were fabricated using a positive photoresist. A 2000 nm Ni film was first sputtered onto the substrate. The photoresist was then applied, exposed, and developed, after which the excess Ni was etched away using diluted nitric acid. Schematics of the Ni-YSZ and Ni-GDC cells are presented in Fig. 1(c) and (d), respectively.

To further investigate the characteristics of Ni-YSZ and Ni-GDC, electrodes of varying sizes were prepared by adjusting the width and number of Ni stripes. The specific parameters are listed in Table 1. Both

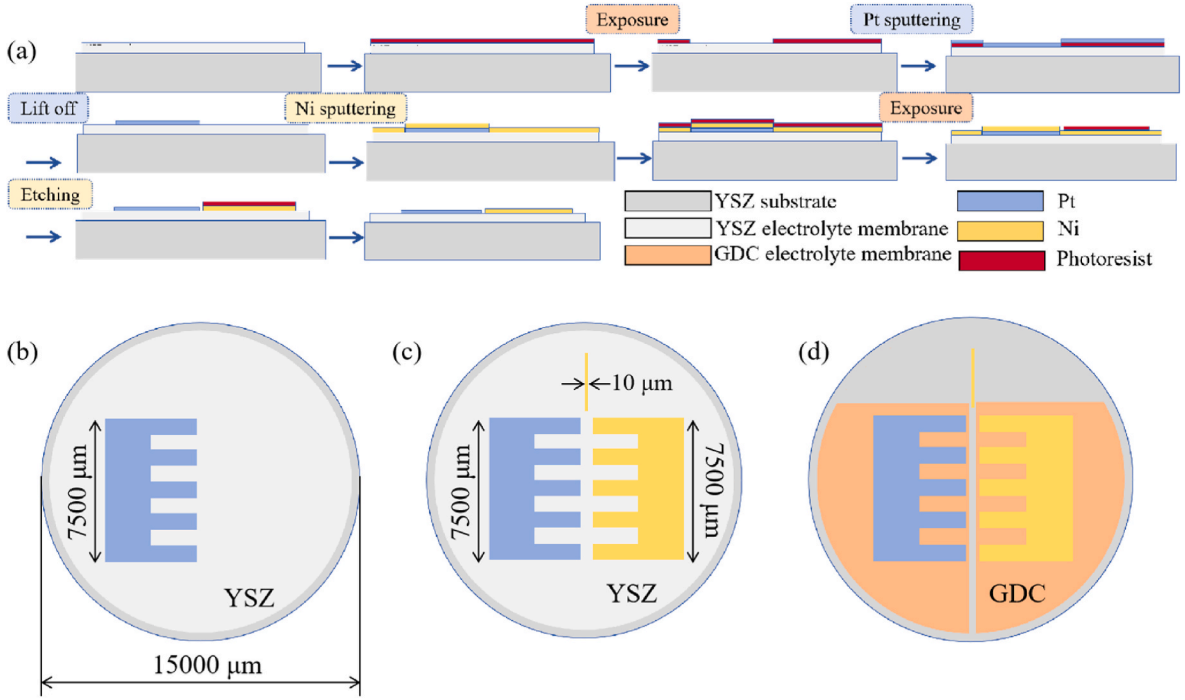

Fig. 1. (a) Schematic of the fabrication process of Ni-YSZ pattern cell; (b) patterned cell only with Pt anode; Schematic of (c) Ni-YSZ patterned cell and (d) Ni-GDC patterned cell.

Table 1
TPB length and Ni electrode area for different-size patterns.

	Parameter
Ni-YSZ/GDC Cell A	TPB: 1.56×10^5 μm Ni area: 7.6×10^6 μm^2
Ni-YSZ/GDC Cell B	TPB: 7.52×10^5 μm Ni area: 7.48×10^6 μm^2
Ni-YSZ/GDC Cell C	TPB: 1.53×10^5 μm Ni area: 1.52×10^6 μm^2

the TPB length and Ni electrode area were calculated only for the stripe region, as shown in Eqs. (1) and (2), excluding the Ni used for collection.

$$\text{TPB length} = \text{number of Ni stripe} \times 2000\ \mu\text{m} \times 2 \quad (1)$$

$$\text{Ni area} = \text{number of Ni stripes} \times 2000\ \mu\text{m} \times \text{width of Ni stripe} \quad (2)$$

Here, 2000 μm represents the total stripe length, and the multiplication by two accounts for the two edges of each stripe. In comparison to Cell A, Cell B features a similar Ni electrode area but a longer TPB length, while Cell C has a comparable TPB length to Cell A but a smaller Ni electrode area.

2.2. Electrochemical measurement

The electrochemical measurements were performed at temperatures of 1073 and 1173 K, using cells placed in quartz glass and alumina chambers, respectively. In both setups, a Pt mesh served as the current collector, and a Pt wire acted as the conductor. The cell and operating conditions are summarized in Table 2 and are described in Fig. S2.

Electrochemical impedance spectroscopy (EIS) and chronoamperometry were conducted using a three-probe measurement setup. For EIS measurements, both an open-circuit voltage (OCV) and a thermal-neutral voltage were applied. The frequency ranged from 1 MHz to 100 mHz, with an amplitude of 100 mV. During impedance fitting, the *Gerischer* element was primarily used to represent reaction polarization resistance, as detailed in a previous study [26]. In addition, chronoamperometry was performed under thermally neutral voltage conditions. During long-term operation, impedance spectra were recorded every 5 h for the first 25 h and every 10 h thereafter. The electrochemical measurements were performed using a Biologic SP-300 (TOYO Corporation, Japan).

2.3. Microstructure observation

Scanning electron microscopy (SEM, JEOL JSM-7001F) and energy-dispersive X-ray spectroscopy (EDX, INCA Oxford Instruments) were employed to examine the cell microstructure and elemental distribution before and after electrochemical measurements. A laser microscope (KEYENCE VK-X3000-300) was used to measure the height distribution of Ni before and after electrochemical measurements. The cell cross-section was polished using a cross-sectional polisher (JEOL SM-09010).

3. Results and discussion

3.1. Effect of temperature on the Ni-YSZ patterned cell operation

A previous study by Bisaka et al. investigated this reaction under different atmospheres at a high temperature of 1173 K [26]. In this study, a thinner YSZ pellet was used as the substrate, resulting in some differences in cell performance, such as smaller polarization resistance and less obvious morphological changes in the Ni stripes in the Ni-YSZ patterned cells.

Table 2
Different operation conditions and equipment.

Equipment	Temperature	Cell	Gas composition
Quartz glass chamber	1073 K	Ni-YSZ	10 %H_2O+1 %H_2+89 %Ar
Alumina chamber	1173 K	Ni-YSZ	10 %H_2O+2 %H_2+88 %Ar
		Ni-GDC	10 %H_2O+2 %H_2+88 %Ar

Fig. 2 and Fig. S3 show the electrochemical performance of the Ni-YSZ patterned cell at 1073 and 1173 K. Fig. 2(a)~(d) present the impedance spectra and corresponding Bode plot at thermoneutral voltage. The results at both temperatures indicate that polarization and ohmic resistances remained relatively stable, with fluctuations observed during the initial 25 h, likely because of the early morphological changes in the material. A slight increase in resistance was observed at the end of the durability test (Fig. 2(e) and Figs. S3(c) and (d)). Moreover, the higher temperature of 1173 K promoted the reaction, resulting in a lower overall polarization resistance than that at 1073 K. As shown in Fig. 2(e), the cell demonstrated a higher current at 1173 K. Additionally, the electrochemical capacitance was calculated, as shown in Fig. 2(f). This likely resulted from the formation of more oxygen vacancies at the YSZ interface at higher temperatures, which facilitated faster reactions and increased chemical capacitance.

Fig. 3 shows the microstructure and morphology of the cells after durability test. The SEM images in Fig. 3(a) and (d) indicate significant differences in the degree of Ni coarsening at different temperatures. At the higher temperature of 1173 K, coarsening was more pronounced, resulting in larger Ni particles compared to those observed at 1073 K. Notably, Ni coarsening does not necessarily lead to the same performance degradation in typical cells. In a typical cell, as Ni particles coarsen, the volume of Ni particles increases and the TPB length decreases. However, in a patterned cell, if the reaction is assumed to occur only at the TPB, coarsening can cause a smooth edge to become curved, potentially increasing the TPB length. Therefore, this morphological evolution of Ni may affect cell performance, particularly during the initial operation.

To observe the interface between the Ni layer and the YSZ substrate, the cross-sections of the cells were polished, as shown in Fig. 3(c) and (f). In Fig. 3(c), the Ni film appears to be closely attached to the YSZ substrate, whereas in Fig. 3(f), a clear gap is visible between the Ni layer and the YSZ substrate. Several hypotheses have been proposed to explain the separation of Ni from the substrate, including a reduction in water vapor concentration, which decreases Ni wettability and promotes detachment [19,23,26], and the accumulation of oxygen vacancies, which includes Ni migration [29–32], among other possibilities [33]. Although the precise cause of delamination remains uncertain, it is evident that a higher operating temperature exacerbates Ni detachment. EDX analysis was performed to investigate the elemental distribution. As shown in Fig. 3(b) and (e), both cell types exhibited Si deposition at the TPB after durability test. This Si deposition may have contributed to the observed increase in polarization resistance during prolonged operation. Although the experiment at 1073 K was conducted in a quartz glass chamber, the one at 1173 K used an alumina chamber and silicon-free rubber rings, making it unlikely that Si originated from the experimental setup. Instead, it may have been introduced through the water used in the experiments. However, the small amount of Si deposition observed is not believed to have significantly affected the morphology change, as the gap between Ni and YSZ and the more pronounced changes in subsequent observations persisted. Furthermore, as shown in Fig. 3(g)–(n), a laser microscope was used to examine the changes in the volume of the Ni layer before and after durability test. Despite the clear gap observed in the cross-sectional SEM image, no significant change in the height distribution was detected. This discrepancy may be due to the change being too subtle to be captured by the laser microscope.

In conclusion, high temperatures accelerated Ni coarsening and led to the detachment of Ni from the YSZ substrate. However, the extent of morphological degradation was insufficient to cause significant changes in the electrochemical performance.

Additionally, the Ni morphology change observed in this study was less drastic than that reported by Bisaka et al. This difference can be attributed to the variation in the cell structure, where the substrate was changed from MgO to YSZ pellets. As sketched in Fig. 4(a), when YSZ is

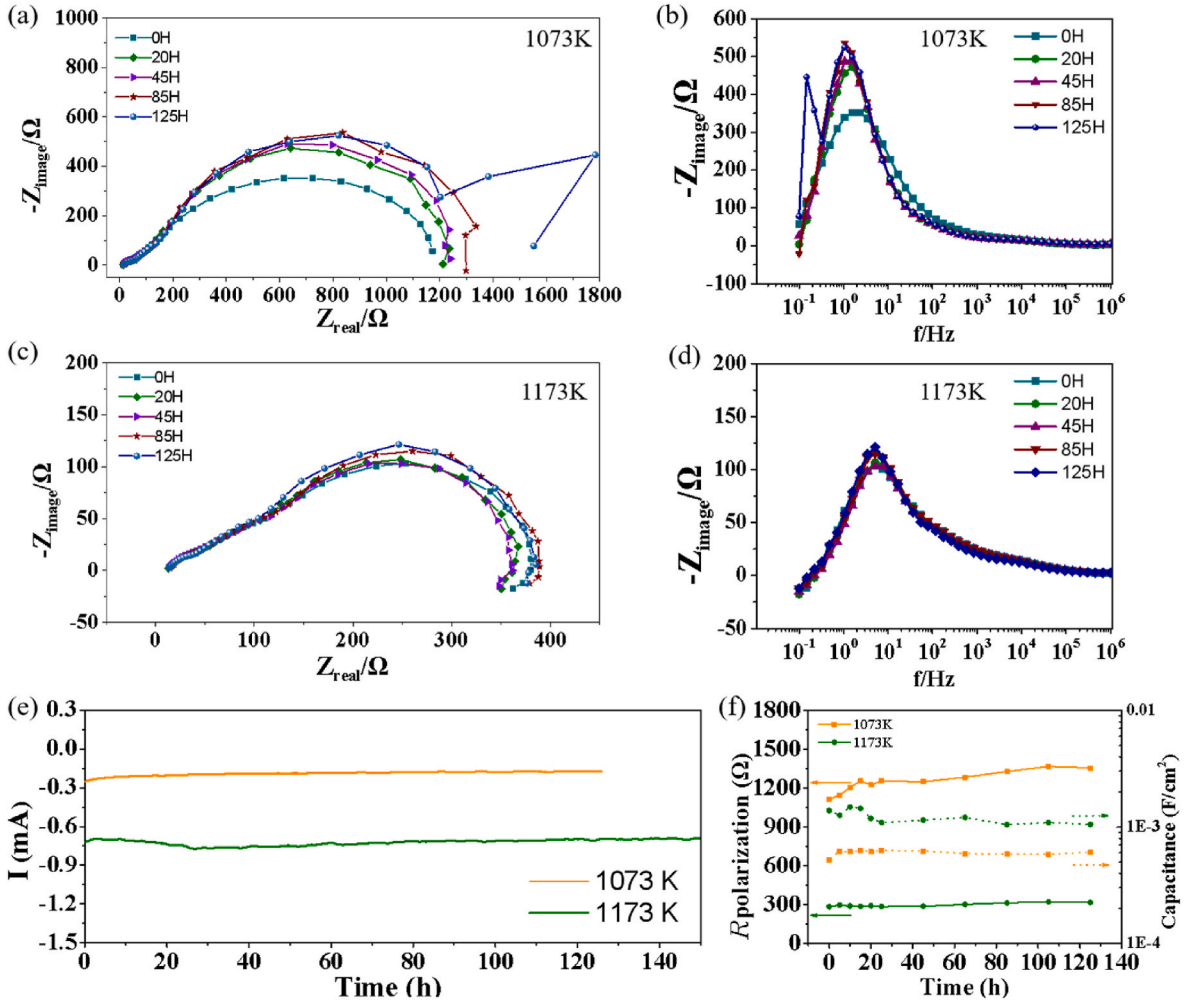

Fig. 2. Ni-YSZ patterned cell impedance spectra and corresponding Bode plot recorded during water electrolysis: (a), (b) at 1073 K and (c), (d) at 1173 K. (e) Time−current curve obtained from chronoamperometry under 1073 and 1173 K. (f) Polarization resistance and electrochemical capacitance trends during long-term operation. Gas condition was 10 %H_2O+1 %H_2+89 %Ar at 1073 K and 10 %H_2O+2 %H_2+88 %Ar at 1173K, respectively.

only a thin film of approximately 800–1000 nm thickness, oxygen ion transport is highly limited. By contrast, increasing the YSZ thickness by approximately 150 times enhances oxygen ion transport through the electrolyte. Therefore, in Fig. 4(b), oxygen ions can flow over a larger area, meaning the reaction region extends from the Ni stripe tip in Fig. 4 (a)–a longer section of the Ni stripe. Firstly, a wider flow range results in more oxygen ions being involved, leading to a higher current. Then, under the same voltage and water vapor concentration, when the reaction area increases, the local degradation can be alleviated.

3.2. *Effect of ceramics in the Ni-ceramic patterned cell*

As discussed in Section 3.1, although a gap between the Ni film and the YSZ substrate is observed at 1173 K, its impact on cell performance is not clearly reflected in the impedance spectra. To exacerbate the degradation and highlight the influence of changes in Ni morphology on cell performance, the experimental parameters were adjusted. Specifically, the width of the Ni stripes was reduced from 100 to 20 μm (Table 1, Cell B) to mimic the particle size of Ni in a typical cell. This section also compares results for different ceramic materials and discusses how their varying properties affect changes in Ni morphology.

3.2.1. *Comparison of electrochemical result between Ni-YSZ and Ni-GDC*

As shown in Fig. 5(a) and (c), Ni-YSZ and Ni-GDC initially exhibited similar impedance spectra, so the same equivalent circuit was used for the initial fitting (Fig. 5(c) ① and ②). However, as the reaction progressed, a third semicircle gradually appeared in the low-frequency region for Ni-GDC. Therefore, a different equivalent circuit was used to fit the subsequent impedance spectra (Fig. 5(e)③). An R-CPE element was used to fit the high-frequency semicircle in both cases. To better understand the high-frequency arc response, the resistances associated with this arc for different cells are shown in Fig. 6. It was observed that the resistance of Ni-YSZ was consistently higher than that of Ni-GDC, suggesting that this component may be related to the electrode reaction. Fig. 7 presents the cross section on patterned cell and 1D transmission line model, which illustrates the fitting strategy and highlights the differences in cell behavior. Here, Ni serves as the electron transport channel, while the ceramic material acts as the ion transport channel. The interface between the two materials, exposed to a gas atmosphere, forms a three-phase boundary. The reactions occurring on both sides of the Ni stripe are represented using *Gerischer* elements. Detailed explanations on Gerischer impedance are provided in the supplementary information. However, the impedance behavior at the head of the stripe deviates from this structure, leading to changes in the impedance shape. The exact physical interpretation of this deviation requires further confirmation; however, it did not exhibit significant changes in size or shape over time, suggesting that it is not related to performance degradation. The characteristic shape of the *Gerischer* element was clearly observed in the mid-frequency range, justifying its use in impedance analysis. In contrast to the Ni-YSZ cell (Fig. 5(e)①), the Ni-

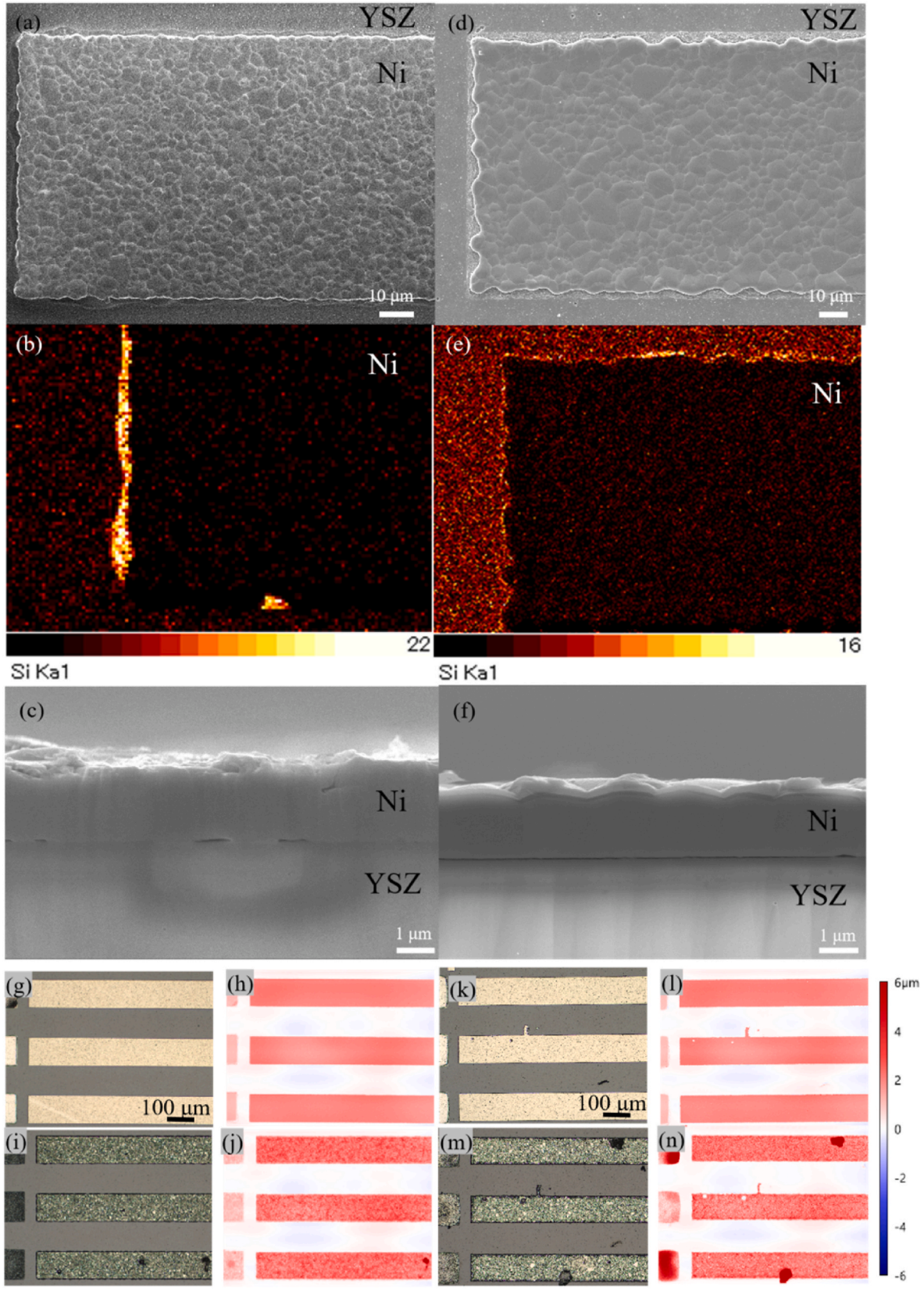

Fig. 3. SEM-EDX images of Ni stripe after durability test at (a), (b)1073 K and (d), (e) 1173 K; Cross section of the cells which operated at (c) 1073 K and (f) 1173 K; (g), (i) and (h), (j) are the height distribution of Ni before and after durability test at 1073 K; (k), (l) and (m), (n) are the height distribution of Ni before and after durability test at 1173 K. On the right is the height distribution scale for (h), (j), (l) and (n). The cell type used here is Ni-YSZ Cell A.

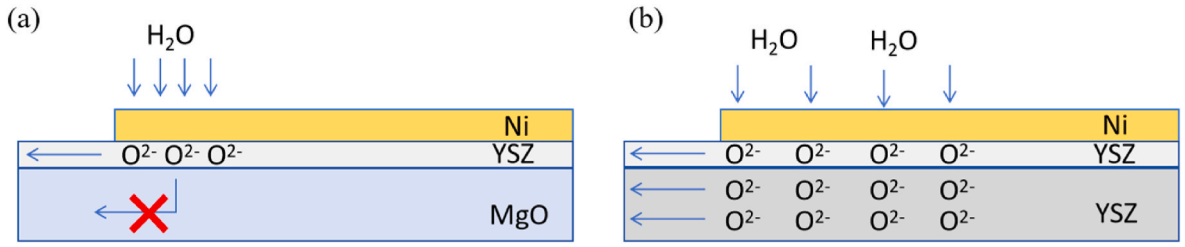

Fig. 4. Reaction diagram of the patterned cells in (a) Bisaka's study [26] and (b) this study.

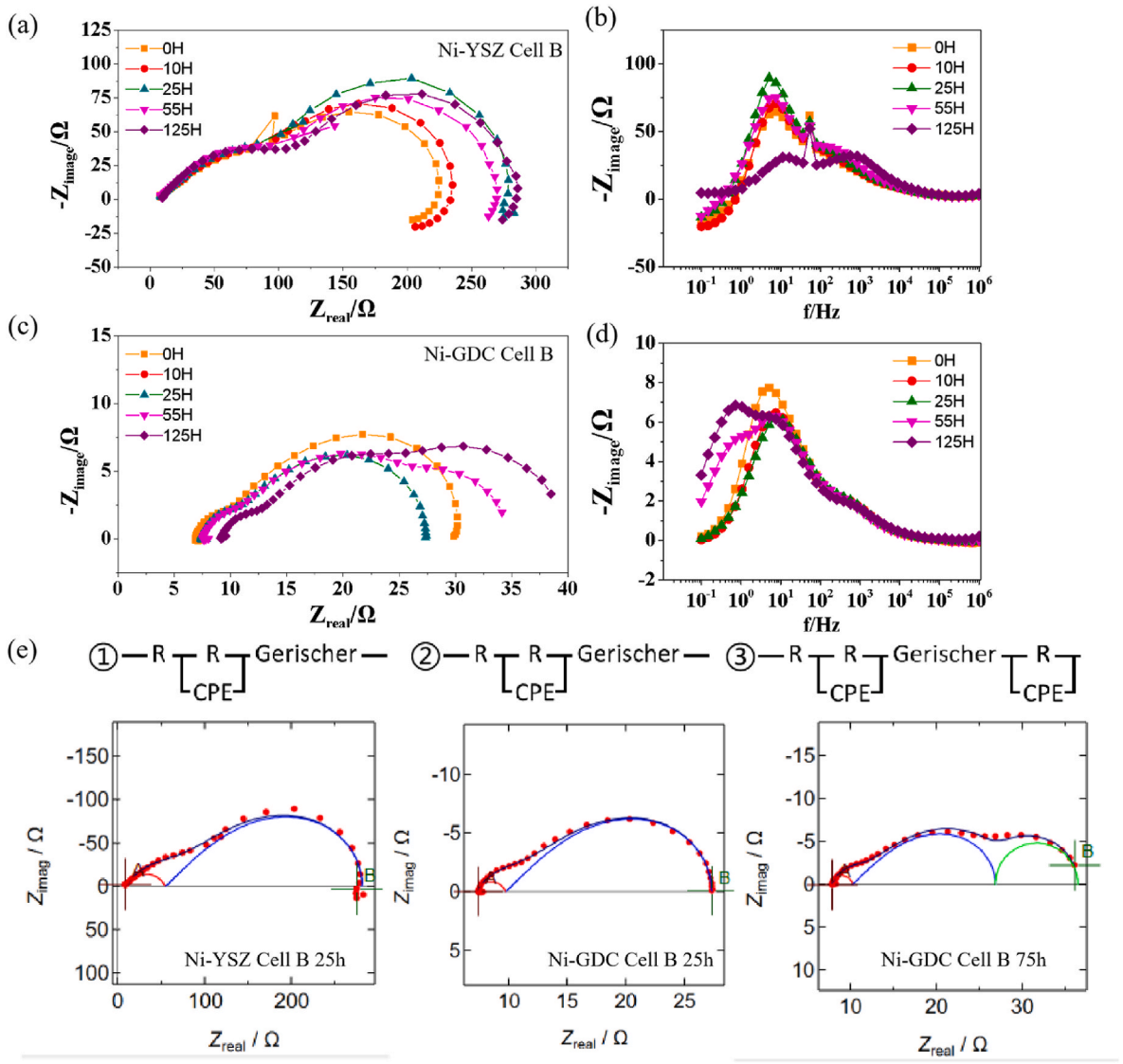

Fig. 5. Impedance spectra and corresponding Bode plot of (a), (b) Ni-YSZ and (c), (d) Ni-GDC cells during the 125h operation; (e) Fitting of impedance spectra with different shapes and corresponding equivalent circuits: ① Ni-YSZ Cell B at 25h, ② Ni-GDC Cell B at 25h, ③ Ni-YSZ Cell B at 75h.

GDC cell shows a new semicircle. This new semicircle appeared at approximately 35 h(Fig. 5(e)③). The physical meaning of this feature is discussed later in this study.

The resistances shown in Fig. 8(a) and (b) were determined by fitting the impedance spectra. For the Ni-YSZ cell (Fig. 8(a)), stable electrochemical performance was maintained, with only a slight increase in polarization resistance observed over time. The Ni-GDC cell (Fig. 8(b)) exhibited a similar trend in polarization resistance; however, its ohmic resistance shifted to the right. Additionally, the emergence and gradual increase in resistance in the low-frequency region from approximately 35 h indicates the onset of a new reaction not observed in the Ni-YSZ cell. The effective reaction lengths in the Ni-YSZ and Ni-GDC cells were calculated based on the polarization resistance derived from the *Gerischer* element (Fig. 8(c)). The effective reaction length was significantly greater in the Ni-YSZ cell than in the Ni-GDC cell. This difference arises because the polarization resistance of the Ni-GDC cell is much smaller, indicating faster reaction kinetics. Consequently, under the same applied potential, the reaction in the Ni-GDC cell was confined to a

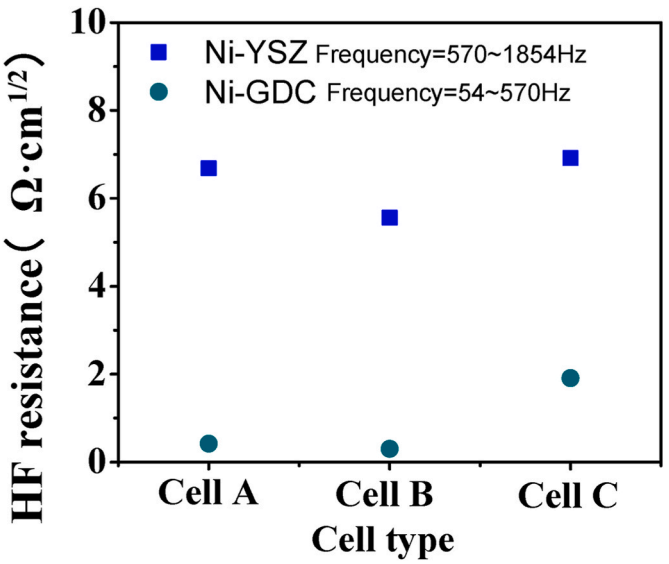

Fig. 6. High frequency resistance in different cells.

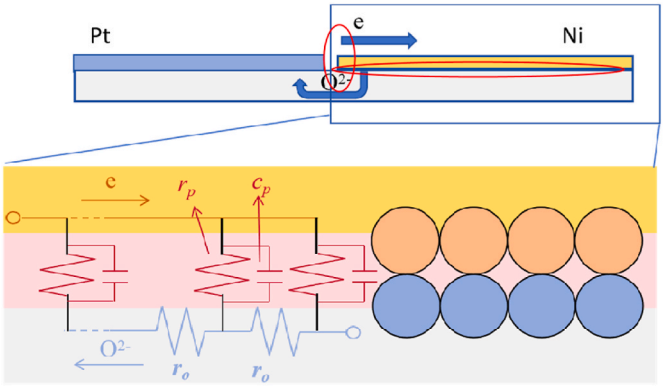

Fig. 7. The cross section on patterned cell and 1D transmission line model. In this model, the electron conduction pathway occurs at Ni, while the ionic conduction pathway occurs at the YSZ or GDC.

shorter reaction length. The chemical capacitances of the Ni-YSZ and Ni-GDC cells are shown in Fig. 8(d). The chemical capacitance of the Ni-GDC cell was markedly higher than that of the Ni-YSZ cell. Considering the differing material properties of YSZ and GDC, the higher chemical capacitance and lower polarization resistance of the Ni-GDC cell can be attributed to the higher concentration of oxygen vacancies at the Ni-GDC interface compared to the Ni-YSZ interface.

3.2.2. *Morphological comparison of Ni-YSZ and Ni-GDC*

Fig. 9 presents the SEM images of the Ni-YSZ and Ni-GDC cells. In Fig. 9(a), after operation, the edges of the Ni stripes in the Ni-YSZ cell become tortuous, and impurities appear along the TPB. This is consistent with the observations in Section 3.1 for Ni-YSZ. The EDX elemental distribution map in Fig. 9(c) confirms the deposition of silica impurities at the TPB. This, coupled with the impedance results, suggests that silica deposition may contribute to the gradual increase in polarization resistance observed during operation. Many studies have reported silica deposition during water electrolysis [34,35]. At high temperatures and high water vapor pressure, $Si(OH)_4$ reaches a significant partial pressure. When electrolysis begins, the equilibrium in reaction (2) shifts. Gaseous $Si(OH)_4$ transforms into silicates and deposits at the TPB. By contrast, Fig. 9(b) shows distinct morphological changes in the Ni-GDC cells. Here, Ni-YSZ and Ni-GDC were tested using the same setup and water vapor source. Significant detachment of Ni was observed, with no obvious impurity deposition at the TPB. In conventional cathode-supported cells, Ni depletion around the electrolyte leads to an increase in ohmic resistance [7,36]. Similarly, in the patterned cell here, delamination at the Ni stripe tips results in a thicker electrolyte, which in turn increases ohmic resistance. Therefore, Ni tip detachment is considered the primary cause of the increased ohmic resistance observed in the Ni-GDC results. Furthermore, the EDX results in Fig. 9(e) show that the GDC layer was completely removed from some areas, eliminating the potential effects of electronic conductivity. Additionally, Fig. 9(d) reveals that silica does not primarily accumulate at the TPB but instead at the interface between GDC and YSZ. This is most likely because the GDC-YSZ interface is the reaction interface closest to the electrolyte. As oxygen ions migrate through the electrolyte, migration resistance arises, causing the applied voltage to gradually decrease. As mentioned earlier, silica deposition is believed to occur alongside water electrolysis [34]. At the location closest to the electrolyte, i.e. the GDC-YSZ interface, the voltage loss due to migration resistance is minimal, leading to a more intense water electrolysis reaction, which in turn results in significant silica deposition. This supports the hypothesis that the reaction extends beyond the TPB to the DPB, which may partly explain the relatively better performance of the Ni-GDC cell. As previously mentioned, a third semicircle appeared in the low-frequency region in Ni-GDC impedance spectrum, which is not observed in the Ni-YSZ cell. This suggests that the low-frequency impedance response in the Ni-GDC cell could be linked to silica deposition at the GDC or GDC-YSZ interface.

Fig. 10 presents laser microscopy images that offer a more intuitive view of the height distribution changes in the two cells. The overall height distribution of the Ni stripes remained largely unchanged, as shown in Fig. 10(a) and (b). However, in Fig. 10(c), similar to the SEM image in Fig. 9(a), the Ni stripe becomes significantly thinner as its height increases. This is primarily due to the coarsening of Ni at high temperatures, where smaller Ni particles aggregate into larger ones, causing morphological changes. In the case of the Ni-GDC cell (Fig. 10 (d) and (e)), a marked difference is observed at the tip of the Ni stripe. The tip shows a pronounced increase in height, indicating Ni detachment at this location. Detachment is most prominent near the electrolyte interface, as confirmed by the SEM images. The laser microscopy analysis further corroborates this, highlighting that detachment initiates at the head of the Ni stripe, which is close to the electrolyte. Finally, similar Ni coarsening behavior was observed in the Ni-GDC cell in Fig. 10(f), where high-temperature operation led to the aggregation of Ni particles, further altering the stripe morphology.

In summary, based on the electrochemical results and morphological characterization, it is speculated that the Ni detachment in Ni-GDC is likely caused by the increased concentration of oxygen vacancies at the GDC interface. This finding aligns with previous studies [29,30]. Although these studies primarily focus on Ni-YSZ electrodes, their calculations indicate that the highest concentration of oxygen vacancies occurs near the electrolyte. This may increase the contact angle between Ni and YSZ, promoting detachment. One study proposed that Ni and ceramic materials bond through Ni–O bonds, and when oxygen vacancies accumulate at the tip of the Ni stripe, where the reaction is most intense, the bond between Ni and the substrate weakens, leading to detachment [29]. The distinct behaviors observed in the Ni-YSZ and Ni-GDC cells in this study further strengthen the hypothesis that oxygen vacancies play a crucial role in this phenomenon.

3.3. *Different reaction regions in the Ni-ceramic patterned cell*

This section explores the reaction regions in Ni-YSZ and Ni-GDC patterned cells by fabricating patterns of varying sizes and examining their electrochemical performance and microstructure.

The parameters for Cells A, B, and C are listed in Table 1. In brief, Cells A and B have similar Ni electrode areas, but the TPB length in Cell

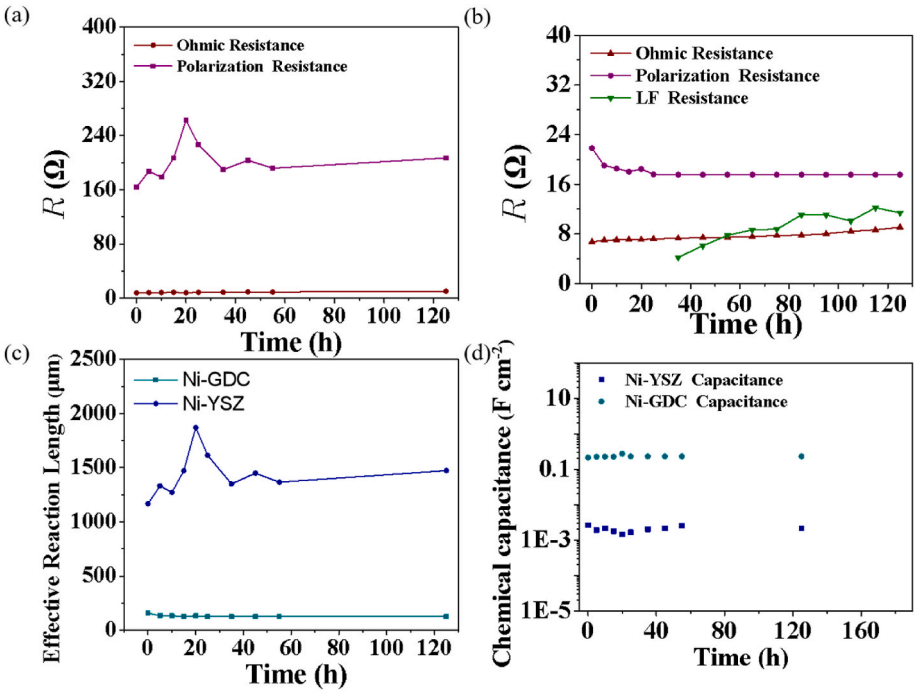

Fig. 8. (a) Ohmic resistance and polarization resistance in Ni-YSZ cell during operation; (b) Ohmic resistance, polarization resistance and low frequency resistance in Ni-GDC cell during operation; (c) Effective reaction length of Ni-YSZ and Ni-GDC cells; (d) Chemical capacitance in Ni-YSZ and Ni-GDC cells.

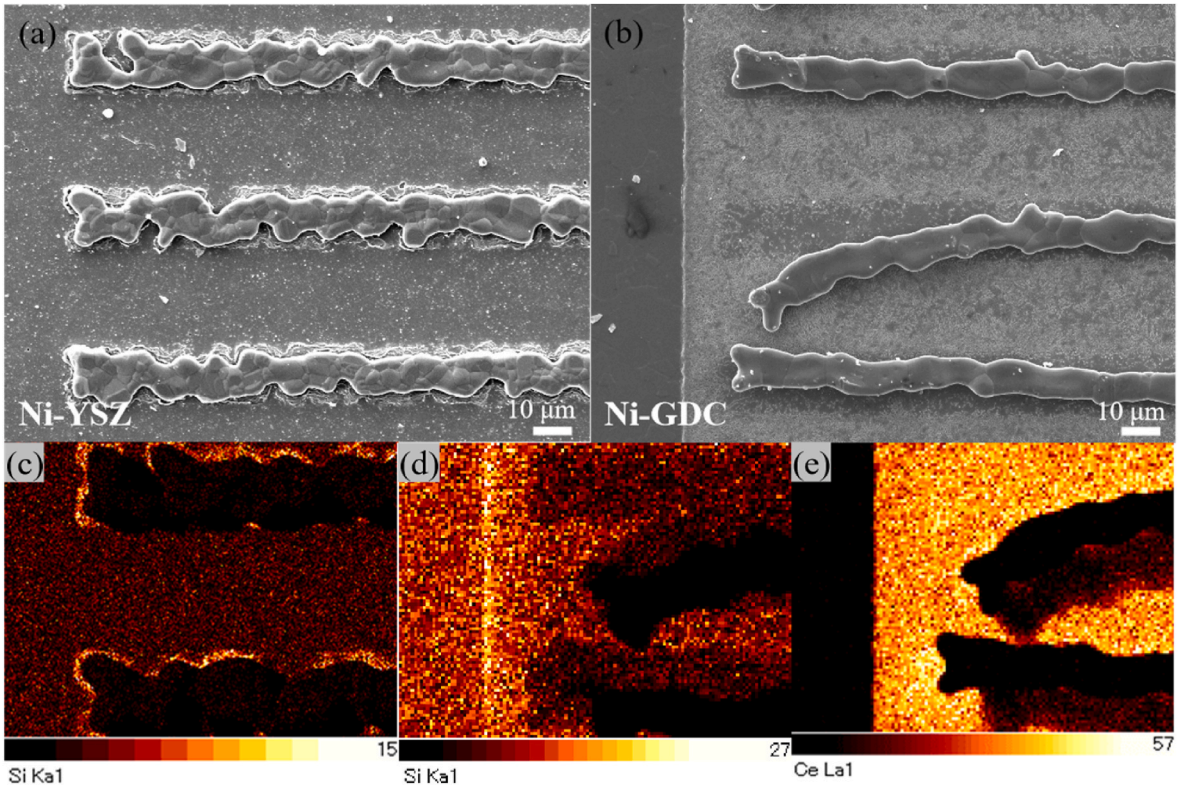

Fig. 9. (a) SEM image and (c) Si element distribution of Ni-YSZ cell after operation; (b) SEM image and (d) Si, (e) Ce elements distribution of Ni-GDC cell after operation, respectively.

A is shorter than in Cell B. Cells A and C have similar TPB lengths, but Cell C has a smaller Ni electrode area. Fig. 11 presents the impedance results for the various cells. Since the Ni-GDC cell substrate in Cell C is one-third thinner than in the other cells (100 vs. 150 μm), the impedance results are normalized. According to Eq. S(8), the polarization resistance was proportional to the square root of the ionic resistance and inversely proportional to the substrate thickness. Therefore, the polarization resistance was normalized by multiplying by the square root of the

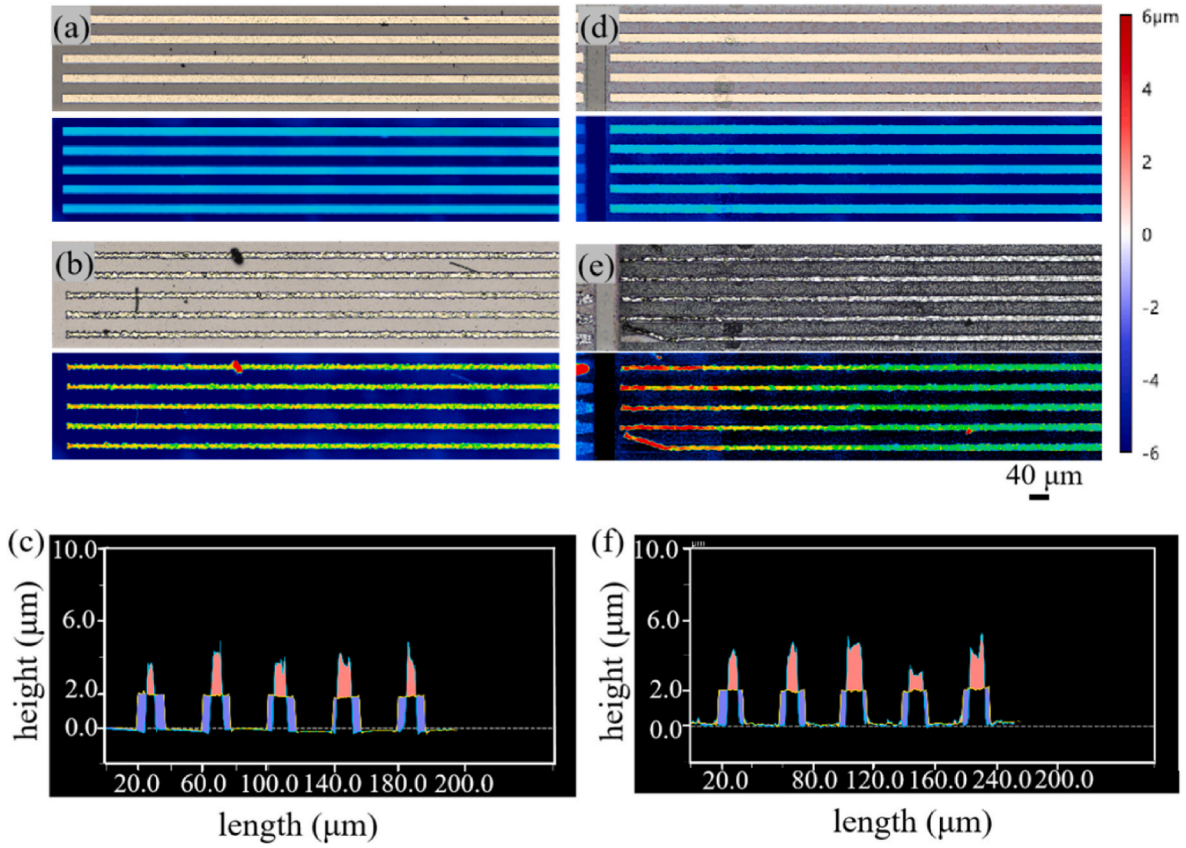

Fig. 10. Laser microscope images and volume height distribution of Ni-YSZ cells (a) before and (b) after durability test; (c) Schematic of Ni stripe width and height height distribution before and after durability test; Laser microscope images and height distribution of Ni-GDC cells (d) before and (e) after durability test; (f) Schematic of Ni stripe width and height distribution before and after durability test. (In (c) and (f), blue means the part missed after durability test, and red means the part presented after durability test). (For interpretation of the references to colour in this figure legend, the reader is referred to the Web version of this article.)

substrate thickness.

Fig. 11(a) and (b) show the Impedance spectra and bode plot for the Ni-YSZ cells with different pattern sizes. To minimize instability due to initial morphology changes or contact issues, impedance spectra after 25 h of electrolysis were analyzed. The data in Fig. 11(e) were derived by fitting the spectra in Fig. 11(a) and normalizing the results. From this analysis, Cell C exhibited the highest ohmic resistance, likely because of its smaller Ni electrode area, which reduced the number of electronic pathways and led to lower electronic conductivity. This resulted in higher ohmic resistance, consistent with the findings in typical cell configurations [37,38]. Additionally, Cell B showed the lowest polarization resistance, likely owing to its increased TPB length.

For the Ni-GDC cells, Cells A and B exhibited nearly identical impedance spectra, as shown in Fig. 11(c). This indicates that, despite a fivefold increase in the TPB length, the polarization resistance of the Ni-GDC-patterned cell did not decrease significantly. However, Cell C showed notable differences before and after normalization, as shown in Fig. 11(f). Before normalization, both polarization and ohmic resistances were higher than those of Cell A. After normalization, the difference in polarization resistance decreased, but the ohmic resistance remained elevated. The overall resistance before normalization was much higher, primarily owing to the thinner substrate with lower ionic conductivity. A thinner electrolyte allows fewer ions to flow, leading to higher ohmic resistance. As shown in the equivalent circuit of Fig. 7 and the calculation of reaction resistance (Eq. S(8)), the resistance of ion transport affects the magnitude of reaction resistance. The higher ion transport resistance can lead to a larger the reaction resistance. After normalization, the polarization resistance was comparable to that of the other cells, indicating that the pattern size did not influence the reaction. The higher ohmic resistance, similar to the results for the Ni-YSZ cells, is likely owing to a reduction in Ni content, leading to lower electronic conductivity [37].

Fig. 12 shows the SEM images of cells with different pattern sizes. Fig. 12(a) and (b) show the Ni-GDC patterned Cells A and C, respectively. Compared to the Ni-YSZ patterned cell of the same size shown in Fig. 3(d), the Ni stripe in Fig. 12(a) did not detach from the substrate, but Ni migration at the edge was significantly more pronounced than in the Ni-YSZ cells. In Fig. 12(b), Ni delaminates from the substrate after durability test, while in Fig. 12(e), which shows a similar pattern for the Ni-YSZ cell, Ni becomes more rugged only at the edges. This comparison highlights that, regardless of pattern size, the Ni-GDC cells exhibited more pronounced morphological changes than the Ni-YSZ cells. Additionally, when the stripe size was reduced to mimic the size of the Ni particles, the Ni layer detached directly from the substrate. Further insights can be obtained from the EDX elemental mapping shown in Fig. 12(c), (d), (f) and (g). Evidently, silica deposition in Ni-GDC is more pronounced at the YSZ-GDC interface, whereas in Ni-YSZ, it mainly occurs in the TPB. Silica deposition can also be observed in the active part of a typical cell [8,39,40]; this suggests that the reaction region extends to the DPB in Ni-GDC, while in Ni-YSZ, it is confined to the TPB.

Fig. 13 summarizes the different degradation phenomena in the Ni-YSZ and Ni-GDC cells. As shown in Fig. 13(a), when a negative potential is applied to the Ni electrode, the potential distribution inside the cell resembles that of a typical cell. As the oxygen ions generated at the head of the Ni stripe travel the shortest distance to the counter electrode, the resulting resistance is minimal, and the potential is closest to the applied potential. As the migration distance increases, the migration resistance rises, causing the local potential to decrease, making it lower than the voltage at the Ni stripe tip. Therefore, the potential at the Ni stripe head is the most negative, the reaction is most intense, the oxygen

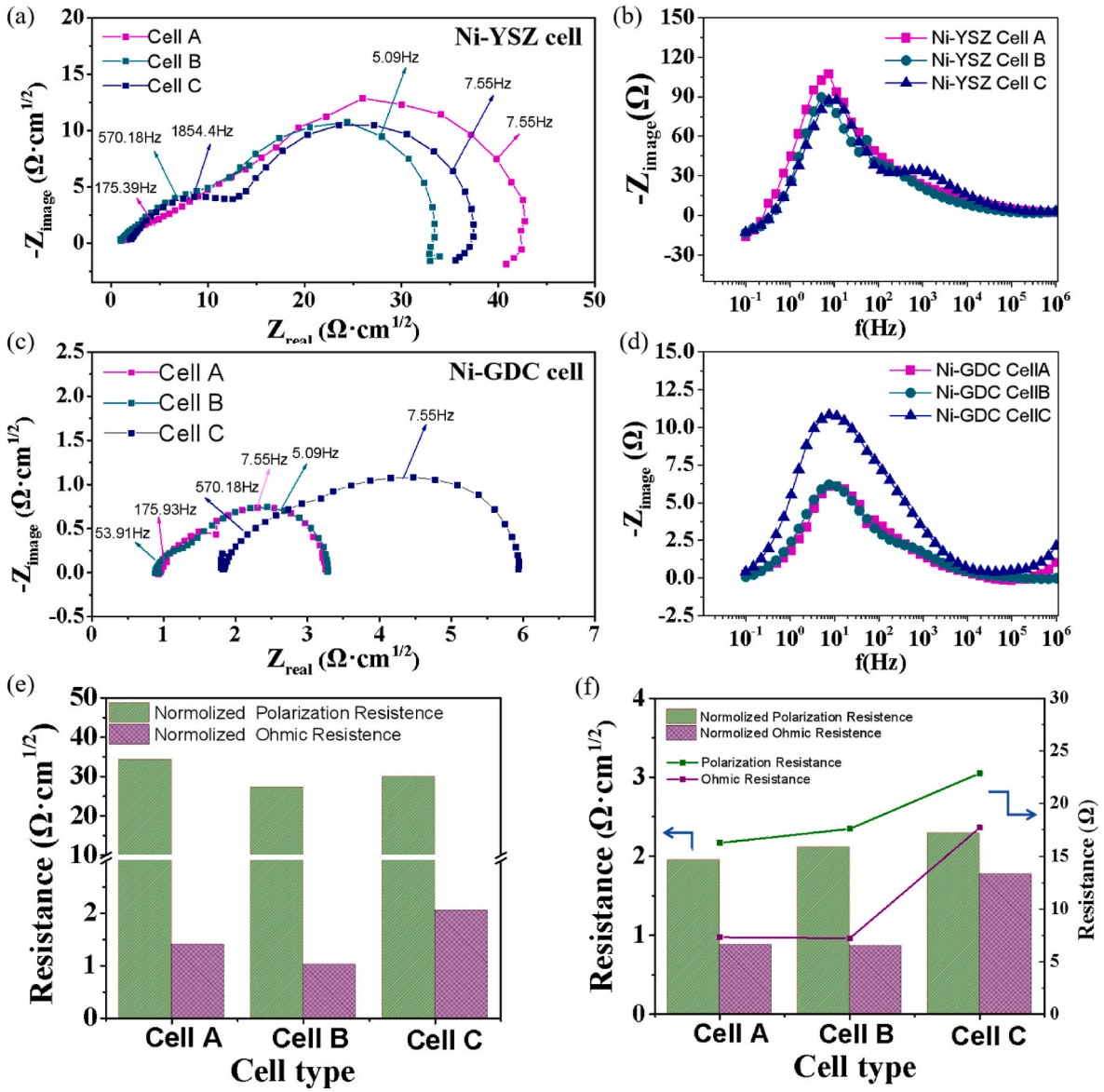

Fig. 11. (a) and (b) Impedance spectra and bode plot of Ni-YSZ Cell A, B and C at 25 h operation; (c) and (d) Impedance spectra and bode plot of Ni-GDC Cell A, B and C at 25 h operation; (e) Normalized polarization resistance and ohmic resistance; (f) Normalized and original polarization resistance and ohmic resistance. Here, Cell A and Cell B have similar Ni electrode areas, but Cell B has a longer TPB. Cell A and Cell C have similar TPB lengths, but Cell A has a larger Ni electrode area.

vacancy concentration formed on GDC is the highest, and eventually, Ni detaches from the head. In addition, significant impurity deposition occurs at the YSZ-GDC interface due to the potential distribution, with the GDC acting as the overall reaction region.

Fig. 13(b) illustrates the degradation process of the Ni-YSZ patterned cell. Since YSZ inherently has fewer oxygen vacancies compared to GDC, Ni does not undergo severe delamination as observed in Ni-GDC cells. However, as discussed in Section 3.1, at higher temperatures, noticeable gaps also appear between Ni and YSZ, which may be due to the higher oxygen vacancy concentration under elevated temperatures. This further suggests that oxygen vacancies could influence Ni morphology changes. Additionally, in Ni-YSZ cells, since the reaction occurs only at the TPB, silica deposition activated by the water vapor electrolysis process and impurity deposits at the Ni-YSZ interface. This deposition is likely the primary reason of the slight degradation observed in Ni-YSZ patterned cells.

4. Conclusions

This study investigated the degradation mechanism of fuel electrodes in SOEC by fabricating comb shaped patterned cells with different ceramic materials: YSZ and GDC films. Electrochemical results and microstructural observations suggest that the slight increase in polarization resistance is likely owing to silica impurity deposition. In the Ni-GDC-patterned cells, Ni stripes near the electrolyte detached, resulting in increased ohmic resistance, while no significant changes were observed in the Ni-YSZ-patterned cell. This difference is likely owing to the higher concentration of oxygen vacancies on the GDC surface.

Additionally, different pattern sizes were used to examine the reaction regions in the Ni-YSZ and Ni-GDC patterned cells. Electrochemical results indicate that the polarization impedance of the Ni-GDC cell is unaffected by the TPB length, suggesting that the reaction may occur at both the GDC and Ni-GDC interfaces. However, while a larger reaction area improves the performance of Ni-GDC cells, they are more susceptible to degradation, such as impurity deposition, compared to YSZ cells, making them more prone to long-term performance degradation.

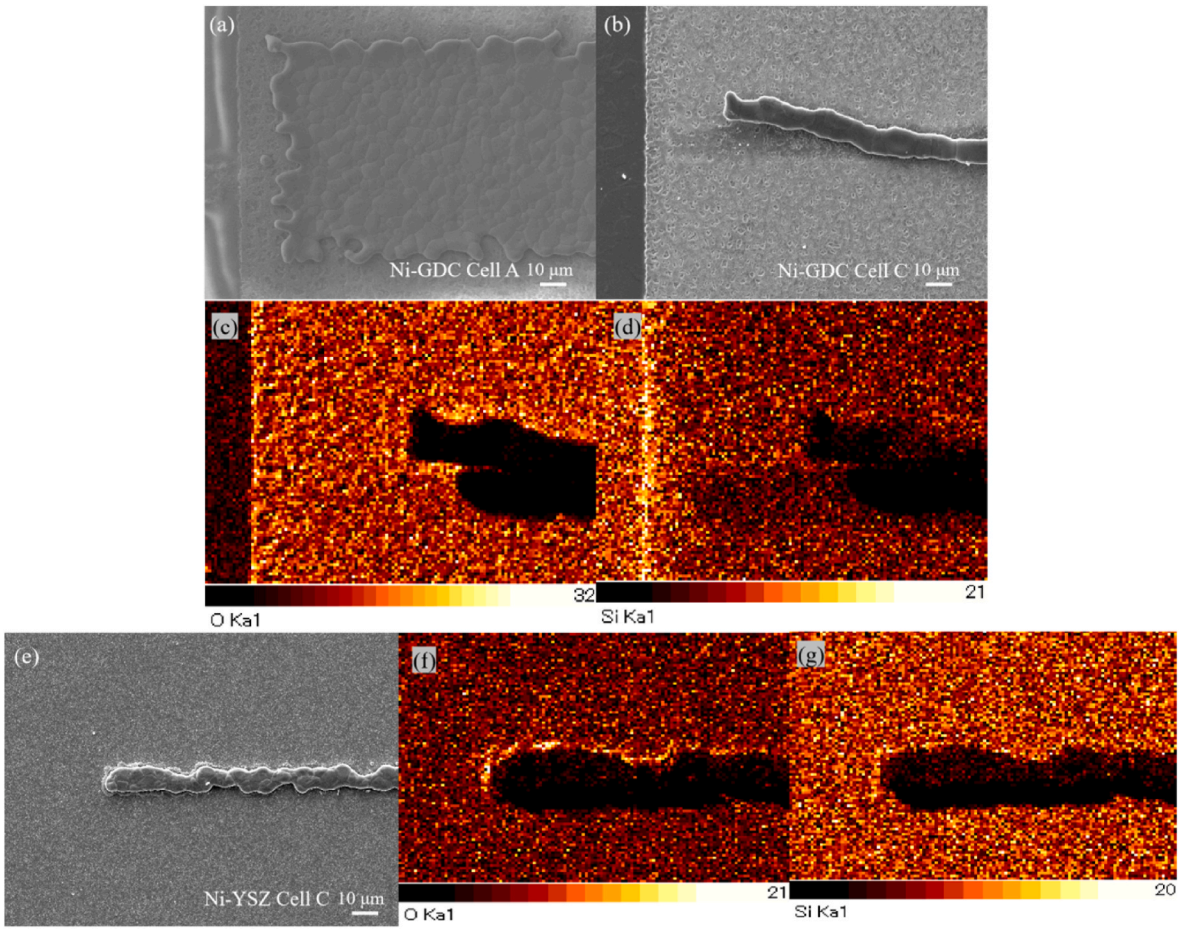

Fig. 12. SEM images of (a) Ni-GDC patterned Cell A, (b) Ni-GDC patterned Cell C and (e) Ni-YSZ patterned Cell C; EDX element mapping of Si and O in (c), (d) Ni-GDC patterned Cell C and (f), (g) Ni-YSZ patterned Cell C, respectively.

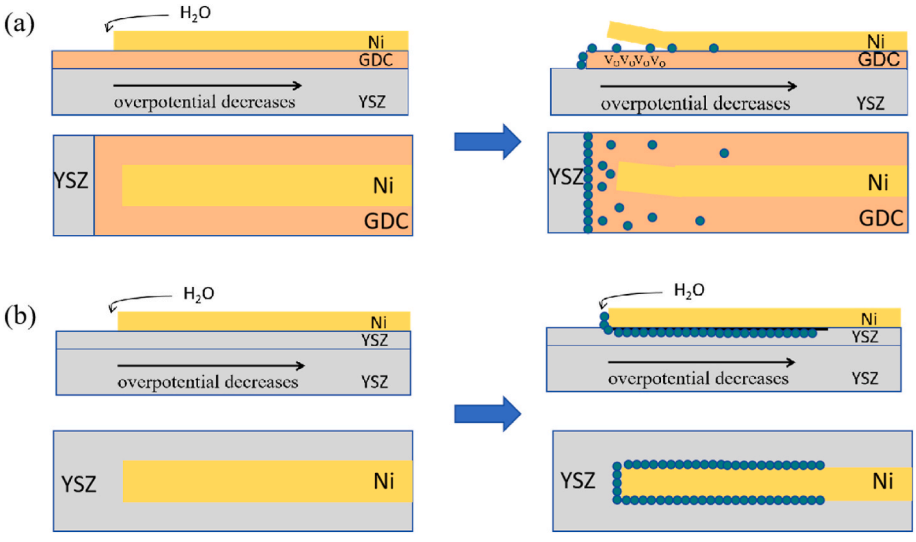

Fig. 13. Degradation diagram of (a) Ni-GDC and (b) Ni-YSZ patterned cells.

CRediT authorship contribution statement

Xiaolin Shao: Writing – original draft, Methodology, Investigation, Formal analysis, Data curation. **Riyan Achmad Budiman:** Writing – review & editing, Supervision, Formal analysis. **Takashi Sato:** Writing – review & editing, Formal analysis. **Mina Yamaguchi:** Writing – review & editing. **Keiji Yashiro:** Writing – review & editing, Supervision, Funding acquisition, Conceptualization. **Tatsuya Kawada:** Writing – review & editing, Supervision, Funding acquisition, Conceptualization.

Declaration of competing interest

The authors declare the following financial interests/personal relationships which may be considered as potential competing interests: Xiaolin Shao reports financial support was provided by Japan Science and Technology Agency. Keiji Yashiro reports financial support was provided by New Energy and Industrial Technology Development Organization. If there are other authors, they declare that they have no known competing financial interests or personal relationships that could have appeared to influence the work reported in this paper.

Acknowledgements

This study was supported by Japan Society for the Promotion of Science (JSPS) KAKENHI (Grant Number JP12KJ3456) and the New Energy and Industrial Technology Development Organization (NEDO), Japan, under a project on the fundamental research and development of liquid synthetic fuel production process technology combining syngas production using renewable energy and the FT reaction (Grant Number JPNP 16002).

Appendix A. Supplementary data

Supplementary data to this article can be found online at https://doi.org/10.1016/j.ijhydene.2025.03.236.

References

[1] Alawad SM, Ben Mansour R, Al-Sulaiman FA, Rehman S. Renewable energy systems for water desalination applications: a comprehensive review. Energy Convers Manag 2023;286:117035.
[2] Irham A, Roslan MF, Jern KP, Hannan MA, Mahlia TMI. Hydrogen energy storage integrated grid: a bibliometric analysis for sustainable energy production. Int J Hydrogen Energy 2024;63:1044–87.
[3] Dincer I, Aydin MI. New paradigms in sustainable energy systems with hydrogen. Energy Convers Manag 2023;283:116950.
[4] Liang WX, Han JT, Zhu WC, Yang JW, Lv W, Liu CH. A novel pathway for achieving efficient integration of SOFC/SOEC and addressing photovoltaic duck curve challenge. Energy Convers Manag 2024;306:118326.
[5] Jolaoso LA, Bello IT, Ojelade OA, Yousuf A, Duan CC, Kazempoor P. Operational and scaling-up barriers of SOEC and mitigation strategies to boost H_2 production- a comprehensive review. Int J Hydrogen Energy 2023;48:33017–41.
[6] Shao X, Budiman RA, Sato T, Yamaguchi M, Kawada T, Yashiro K. Review of factors affecting the performance degradation of Ni-YSZ fuel electrodes in solid oxide electrolyzer cells. J Power Sources 2024;609:234651.
[7] Hoerlein MP, Riegraf M, Costa R, Schiller G, Friedrich KA. A parameter study of solid oxide electrolysis cell degradation: microstructural changes of the fuel electrode. Electrochim Acta 2018;276:162–75.
[8] Mogensen MB, Chen M, Frandsen HL, Graves C, Hauch A, Hendriksen PV, et al. Ni migration in solid oxide cell electrodes: review and revised hypothesis. Fuel Cells 2021;21:415–29.
[9] Hu F, Ling YH, Fang SY, Sui LT, Xiao HW, Huang YL, et al. Engineering dual-exsolution on self-assembled cathode to achieve efficient electrocatalytic CO_2 reduction. Appl Catal B Environ 2023;337:122968.
[10] Du Y, Zhao L, Xiao Y, Kong J, Liu P, Yang X, et al. High electrolysis performance of the SOEC cathode by creating oxygen vacancies to regulate the adsorption energy. J Mater Chem A 2024;12:28911–8.
[11] Kaur T, Singh K, Kolte J. Effect of intrinsic and extrinsic oxygen vacancies on the conductivity of Gd-doped CeO_2 synthesized by a sonochemical route. J Phys Chem C 2022;126:18018–28.
[12] Sivasankaran V, Combemale L, François M, Caboche G. $Ce_{0.9}Gd_{0.1}O_{2-x}$ for intermediate temperature solid oxide fuel cells: influence of cathode thickness and anode functional layer on performance. Energies 2020;13:4400.
[13] Chueh WC, Hao Y, Jung W, Haile SM. High electrochemical activity of the oxide phase in model ceria–Pt and ceria–Ni composite anodes. Nat Mater 2012;11:155–61.
[14] Sciazko A, Shimura T, Komatsu Y, Shikazono N. Ni-GDC and Ni-YSZ electrodes operated in solid oxide electrolysis and fuel cell modes. J Therm Sci Technol 2021;16:1–10.
[15] Mewafy B, Paloukis F, Papazisi KM, Balomenou SP, Luo W, Teschner D, et al. Influence of surface state on the electrochemical performance of nickel-based cermet electrodes during steam electrolysis. ACS Appl Energy Mater 2019;2:7045–55.
[16] Li W, Shi Y, Luo Y, Wang Y, Cai N. Carbon deposition on patterned nickel/yttria stabilized zirconia electrodes for solid oxide fuel cell/solid oxide electrolysis cell modes. J Power Sources 2015;276:26–31.
[17] Li W, Shi Y, Luo Y, Wang Y, Cai N. Carbon monoxide/carbon dioxide electrochemical conversion on patterned nickel electrodes operating in fuel cell and electrolysis cell modes. Int J Hydrogen Energy 2016;41:3762–73.
[18] Doppler MC, Fleig J, Bram M, Opitz AK. Hydrogen oxidation mechanisms on Ni/yttria stabilized zirconia anodes: separation of reaction pathways by geometry variation of pattern electrodes. J Power Sources 2018;380:46–54.
[19] Jiao Z, Shikazono N. Study on the effects of polarization on local morphological change of nickel at active three-phase-boundary using patterned nickel-film electrode in solid oxide fuel cell anode. Acta Mater 2017;135:124–31.
[20] Jiao Z, Shikazono N. In operando optical study of active three phase boundary of nickel-yttria stabilized zirconia solid-oxide fuel cell anode under polarization. J Power Sources 2018;396:119–23.
[21] Jiao Z, Busso E P, Shikazono N. Influence of polarization on the morphological changes of nickel in fuel electrodes of solid oxide cells. J Electrochem Soc 2020;167:024516.
[22] Ouyang Z, Komatsu Y, Sciazko A, Katsuhiko N, Shikazono N. In-Operando observations of Ni-YSZ patterned fuel electrodes under SOFC and SOEC operations. ECS Trans 2021;103:1219.
[23] Ouyang ZF, Komatsu Y, Sciazko A, Onishi J, Nishimura K, Shikazono N. Operando observations of active three phase boundary of patterned nickel- Yttria stabilized zirconia electrode in solid oxide cell. J Power Sources 2022;529:231228.
[24] Komatsu Y, Sciazko A, Suzuki Y, Ouyang Z, Jiao Z, Shikazono N. Operando observation of patterned nickel - gadolinium doped ceria solid oxide fuel cell anode. J Power Sources 2021;516:230670.
[25] Yao G, Okabe T, Shikazono N. Ni migration on porous yttria-stabilized zirconia and yttria-micropatterned fuel electrodes in solid oxide fuel cells. J Power Sources 2024;609:234720.
[26] Bisaka N, Sato T, Budiman RA, Yamaguchi M, Kawada T, Yashiro K. Microstructure alteration analysis of Ni/YSZ cermet by comb-shaped Ni patterned electrode. J Electrochem Soc 2024;171:104510.
[27] Trini M, Hauch A, De Angelis S, Tong X, Hendriksen PV, Chen M. Comparison of microstructural evolution of fuel electrodes in solid oxide fuel cells and electrolysis cells. J Power Sources 2020;450.
[28] Enrique R, Joachim M. Electronic transport in single crystals of gddoped ceria. ECS Trans 2007;2:51–61.
[29] Monaco F, Hubert M, Vulliet J, Ouweltjes JP, Montinaro D, Cloetens P, et al. Degradation of Ni-YSZ electrodes in solid oxide cells: impact of polarization and initial microstructure on the Ni evolution. J Electrochem Soc 2019;166:F1229.
[30] Rorato L, Shang Y, Yang S, Hubert M, Couturier K, Zhang L, et al. Understanding the Ni migration in solid oxide cell: a coupled experimental and modeling approach. J Electrochem Soc 2023;170:034504.
[31] Shang YJ, Smitshuysen AL, Yu M, Liu YL, Tong XF, Jorgensen PS, et al. 3D microstructural characterization of Ni/yttria-stabilized zirconia electrodes during long-term CO_2 electrolysis. J Mater Chem A 2023;11:12245–57.
[32] Weber MLJD, Fearn S, Cavallaro A, Prochazka M, Gutsche A, et al. Thermal stability and coalescence dynamics of exsolved metal nanoparticles at charged perovskite surfaces. ChemRxiv 2023;15:9724.
[33] Mogensen MB, Mogensen G. (Invited) on degradation mechanisms of Ni-YSZ fuel electrodes in solid oxide cells. ECS Trans 2023;112:71.
[34] Hauch A, Ebbesen SD, Jensen SH, Mogensen M. Solid oxide electrolysis cells: microstructure and degradation of the Ni/Yttria-Stabilized zirconia electrode. J Electrochem Soc 2008;155:B1184.
[35] Shimura T, Jiao ZJ, Shikazono N. Polarization characteristics and microstructural changes of solid oxide fuel cell and solid oxide electrolysis cell fuel electrodes. J Electrochem Soc 2017;164:F1158–64.
[36] The D, Grieshammer S, Schroeder M, Martin M, Al Daroukh M, Tietz F, et al. Microstructural comparison of solid oxide electrolyser cells operated for 6100 h and 9000 h. J Power Sources 2015;275:901–11.
[37] Keane M, Fan H, Han MF, Singh P. Role of initial microstructure on nickel-YSZ cathode degradation in solid oxide electrolysis cells. Int J Hydrogen Energy 2014;39:18718–26.
[38] Vafaeenezhad S, Hanifi AR, Laguna-Bercero MA, Etsell TH, Sarkar P. Microstructure and long-term stability of Ni–YSZ anode supported fuel cells: a review. Materials Futures 2022;1:042101.
[39] Tian J, Milcarek RJ. Siloxane deposition on the Ni-YSZ solid oxide fuel cell anode exposed to bio-syngas. J Electrochem Soc 2021;168:044503.
[40] Zhou Y, Wei F, Wu H. Fe-decorated on Sm-doped CeO_2 as cathodes for high-temperature CO2 electrolysis in solid oxide electrolysis cells. Electrochim Acta 2022;419:140434.